SCIENTIFIC REPORTS
nature research

OPEN

Long-range propagation of protons in single-crystal VO_2 involving structural transformation to HVO_2

Keita Muraoka & Teruo Kanki*

Vanadium dioxide (VO_2) is a strongly correlated electronic material with a metal-insulator transition (MIT) near room temperature. Ion-doping to VO_2 dramatically alters its transport properties and the MIT temperature. Recently, insulating hydrogenated VO_2 (HVO_2) accompanied by a crystal structure transformation from VO_2 was experimentally observed. Despite the important steps taken towards realizing novel applications, essential physics such as the diffusion constant of intercalated protons and the crystal transformation energy between VO_2 and HVO_2 are still lacking. In this work, we investigated the physical parameters of proton diffusion constants accompanied by VO_2 to HVO_2 crystal transformation with temperature variation and their transformation energies. It was found that protons could propagate several micrometers with a crystal transformation between VO_2 and HVO_2. The proton diffusion speed from HVO_2 to VO_2 was approximately two orders higher than that from VO_2 to HVO_2. The long-range propagation of protons leads to the possibility of realizing novel iontronic applications and energy devices.

Controlling the properties of strongly correlated electronic materials *via* carrier and impurity doping has gained significant attention over the past years. Doping has an impact on 3*d*-band filling, which often results in dramatic modification of the orbital states. This results in large changes of electronic properties, such as the metal-insulator transition (MIT). For example, a shift of the MIT temperature (T_{MI}) of VO_2 *via* doping with a variety of elements, such as W, Mo, and Nb has been reported[1–8]. This is caused by charge transfer from the impurity ions to the vanadium ions through the oxygen ions, which displaces an integral number of $3d^1$ electrons in V^{4+} that are Mott insulating states to $3d^{1+\delta}$, resulting in the formation of more stable metallic states. When using impurity elements with large atomic numbers of W, Mo and Nb, however, it is impossible to dynamically control the number of mobile carriers because of solid-state materials determined by an initial doping level. On the other hand, protons having strongly reductive activity in oxide materials can dynamically move *via* external fields and function as an electron donor. Recent work has demonstrated that dynamic proton-intercalation results in a large, reversible resistance modulation in oxide thin films, such as $SrTiO_3$, $NdNiO_3$, and VO_2 *via* a catalytic effect[9–13], a non-catalytic effect[14,15], or an electric field[16–20]. In general, the intercalation of protons in the insulating VO_2 state decreases its resistivity and it approaches a metallic state with a pseudo rutile structure[11,19,21–24]. According to Yoon *et al.*[13], heavy doping with protons using Pt catalytic nano-particles transforms VO_2 into HVO_2 under an $H_2 + Ar$ gas atmosphere. HVO_2 has a different crystal structure from the tetragonal VO_2, and it demonstrates typical-insulating behavior that follows the Arrhenius equation with a higher resistivity than that of VO_2. Moreover, a reversible structural deformation is possible between VO_2 in air and HVO_2 in the $H_2 + Ar$ gas atmosphere. This reversible resistance change has the potential to lead to the realization of novel ionic and/or electronic applications. However, there is lack of information regarding essential physical parameters in this system, such as the diffusion constant of the intercalated protons in VO_2 and the crystal transformation energy between VO_2 and HVO_2.

In this work, we demonstrated the long-range propagation of protons in VO_2. This was accomplished by investigating the transient electronic transport properties during proton intercalation in VO_2 and the associated structural transformation to HVO_2 under $H_2 + Ar$ gas atmosphere. This was followed by a return to VO_2 from HVO_2 after proton desorption under an N_2 gas atmosphere. The results showed that the diffusion constants and crystal transformation energies differed for the two states.

Institute of Scientific and Industrial Research, Osaka University, 8-1 Mihogaoka, Ibaraki, Osaka, 567-0047, Japan. *email: kanki@sanken.osaka-u.ac.jp

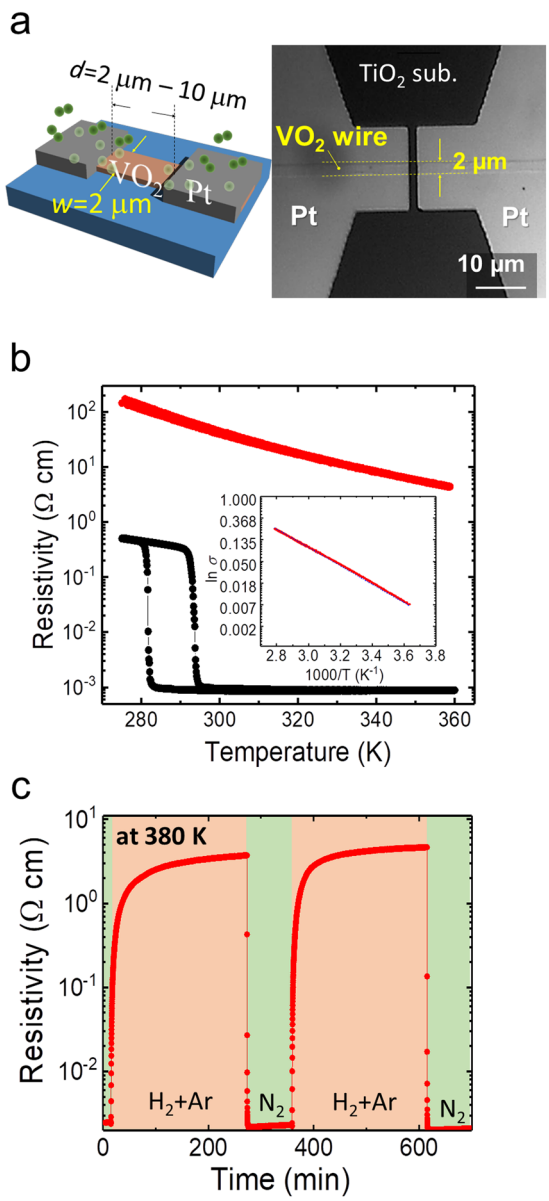

Figure 1. VO_2 microwire device with Pt electrode with catalytic effect and Basic transport properties of VO_2 and heavily proton intercalated VO_2. (**a**) A schematic illustration (left) and an optical microscope image (right) of a VO_2 microwire for the proton intercalation experiment. (**b**) Temperature dependence of the resistivity curves of a pristine 4-μm-length VO_2 wire (the black solid dots) and of hydrogenated VO_2 (HVO_2) (the red solid dots). The inset shows the $1/T$ dependence of ln σ for the Arrhenius plots (**c**) The reversibility of the transport properties under $H_2 + Ar$ or N_2 gases at 380 K.

Results

Device structures and basic transport properties. For VO_2 microwire devices prepared on TiO_2 (001) substrates, the width (w) was fixed at 2 μm and the distance between catalytic Pt electrodes (d) was from 2 μm to 10 μm, as shown in the schematic in Fig. 1a. The optical image on the right of Fig. 1a shows a VO_2 microwire with Pt electrodes as an example. Figure 1b shows the temperature dependence of the resistivity curves in a VO_2 microwire with $d = 4$ μm. The pristine VO_2 shows typical electronic transport properties with hysteresis due to the MIT in a N_2 gas atmosphere (solid black dots). Continuous annealing under $H_2(5\%) + Ar(95\%)$ gas at 380 K for ~5 h resulted in a marked change to the insulating phase that followed the Arrhenius equation (solid red dots). The resistivity increased by ~5 orders of magnitude, which is in agreement with ref. [13]. They determined that the heavily hydrogenated VO_2 had a structural deformation to HVO_2, which resulted in a ~10% expansion in the [100] direction of the rutile VO_2 structure and opened a band gap calculated by a first-principle method[13]. The band gap (E_g) of the hydrogenated HVO_2 was 0.71 eV, as derived from the inset of Fig. 1b using the equation as a pure semiconductor $\ln\sigma = -\frac{E_g}{2k_B}\frac{1}{T} + \ln\sigma_0$, where σ, σ_0, and k_B are the conductivity of the thin film, a constant,

and the Boltzmann constant, respectively. The E_g takes the half value with the calculated bandgap of the HVO_2 with 2 electron doping unit cell in ref. [13]. Furthermore, these results indicate that the VO_2 microwires also become fully hydrogenated VO_2 in the 4 μm gap between the Pt source and drain catalytic electrodes. Figure 1c shows the reversibility of the transport properties under H_2+Ar or N_2 gases at 380 K. The VO_2 microwire was initially metallic at 380 K in a N_2 atmosphere. As soon as H_2 gas was introduced into the measurement cell, the resistivity promptly increased with the intercalation of protons into VO_2. Eventually, the H_2 gas annealing resulted in the heavily hydrogenated VO_2, i.e., it formed the insulating HVO_2 phase. Compared with the time required for the transformation from VO_2 to HVO_2, the HVO_2 phase returned to the initial metallic VO_2 more quickly on N_2 gas annealing. This trend was in agreement with the data from ref. [13]. The results of this experiment revealed the micro-scale diffusion of protons with a crystal change from VO_2 to HVO_2. Regarding repeatability of electronic property of VO_2 thin films after N_2 annealing at 380 K from HVO_2, the temperature dependence of resistance curves is almost same as the pristine curve, keeping the framework of VO_2 (Please see the section E in Supplementary Information in detail).

Analysis of the transient resistance behavior. Based on the H_2 or N_2 atmosphere dependent reversible reaction, the evolution of the proton concentration in VO_2 with time was investigated. As a boundary condition between the Pt and VO_2 interface, the chemical reaction rate as a differential equation with respect to time (t) was introduced according to:

$$\frac{dn_{\text{inter}}}{dt} = k_1 n_{\text{H+}} - k_2 n_{\text{inter}} \tag{1}$$

where k_1 and k_2 are the forward and reverse reaction rate constants, respectively, $n_{\text{H+}}$ is the proton concentration at the contact area between the Pt catalytic electrodes and VO_2, and n_{inter} is the proton concentration at the VO_2 interface. From Eq. (1), the behavior of Fig. 1c can be understood. In the beginning, protons are intercalated into VO_2 at the contact points between Pt, VO_2, and the H_2 + Ar gas phase, as seen in an upper illustration of Fig. 2a, because $k_1 n_{\text{H+}} > k_2 n_{\text{inter}}$, and $n_{\text{inter}} = 0$ during the initial stage. The value of $k_2 n_{\text{inter}}$ gradually approaches that of $k_1 n_{\text{H+}}$, until the two values are finally equal and reach the equilibrium state. As the H_2 + Ar gas is changed to N_2, $n_{\text{H+}}$ approximately becomes zero, thus the protons in VO_2 are removed and the insulating HVO_2 returns to the metallic VO_2 form. This dynamic reaction at the interface was taken as a boundary condition with a dynamic time-dependence in the simulation below.

Next, we consider how the intercalated protons diffuse in VO_2. Theoretically, for ion diffusion, the ionic fluxes likely arise from a gradient in the ion concentration in the solid-state material. Thus, since n_{HVO2} is the proton ratio in a VO_2 unit cell, the hydrogen ion flux (J_{HVO2}) can be described as: $J_{\text{HVO2}} = -D\nabla n_{HVO2}$, where D is the diffusion coefficient. To conduct the transient state analysis, we use Fick's second law in the one dimensional case, namely, $\frac{\partial n_{HVO2}}{\partial t} = -\frac{\partial J_{HVO2}}{\partial x}$, which predicts the spatiotemporal evolution of the ion concentration. With this the following equation was obtained:

$$\frac{\partial n_{HVO2}}{\partial t} = -D\frac{\partial^2 n_{HVO2}}{\partial x^2}. \tag{2}$$

To evaluate the spatiotemporal evolution of the proton concentration in VO_2, numerical analysis using the finite difference method (FDM) was carried out based on the boundary condition of Eq. (1) and the transient diffusion equation of Eq. (2) (see Section A in Supplementary Information).

The inset of Fig. 2b shows the spatiotemporal mapping of the proton density in VO_2 from the simulation with $D = 150$ nm^2/s. Here, $x = 0$ represents the interface of the VO_2 contacted with the Pt electrodes. We divided the 2-μm-length VO_2 wire by 100 in the FDM calculation, thus the integral i goes from 1 to 100 and the divided length (Δx) is 20 nm (further details in Section A of the Supplementary Information). The inset of Fig. 2b represents the proton diffusion behavior of a 4-μm-length VO_2 wire because the intercalation and diffusion behavior becomes symmetric at a 2 μm distance from the Pt electrodes. Through this analysis, we can clearly understand the transient behavior of proton diffusion in the VO_2 wires.

For conversion of the proton concentration in VO_2 to resistivity, a serial resistor model was used as shown in the lower illustration of Fig. 2a, which is represented by the following equation:

$$\rho(T) = \frac{1}{100}\sum_{i=1}^{100}\rho_i(T) \tag{3}$$

The $\rho_i(T)$ can be simply defined as $(1 - n_{HVO2})\rho_i^{VO2} + n_{HVO2}\rho_i^{HVO2}(T)$, where ρ_i^{VO2} is the resistivity of metallic VO_2 and $\rho_i^{HVO2}(T)$ is the temperature dependent resistivity of the insulating HVO_2.

The ρ_i^{VO2} was fixed at 0.0008 Ω cm between 300 K and 380 K because of its nearly constant value with reference to the VO_2 resistivity curve in Fig. 1c, while $\rho_i^{HVO2}(T)$ varies with temperature. The experimental values of $\rho_i^{HVO2}(T)$ were taken at the required temperature by referring to the temperature vs resistance curve of HVO_2 in Fig. 1b. Figure 2b shows the transient resistivity behavior with time for the 4-μm-, 6-μm-, and 10-μm-length VO_2 wires at 380 K. The red dot curves show the simulation results using Eqs. (1) to (3) with the appropriately selected diffusion constant for the proton that transforms the crystal structure from VO_2 to HVO_2; $D_{\text{HVO2}} = 150$ nm^2/s at 380 K determined by the wire lengths of VO_2 with 4 μm, 6 μm, and 10 μm. The simulation curves could fit to the experimental curves well in their lengths. The diffusion value was compared with proton diffusion in the [001] direction of rutile-type TiO_2 without a structural transformation[25]. It is considered that the slower diffusion constant of VO_2 [110] than that of TiO_2 [001] would be due to difference of two oxygen distance ($d_{o\text{-}o}$) in [001] and

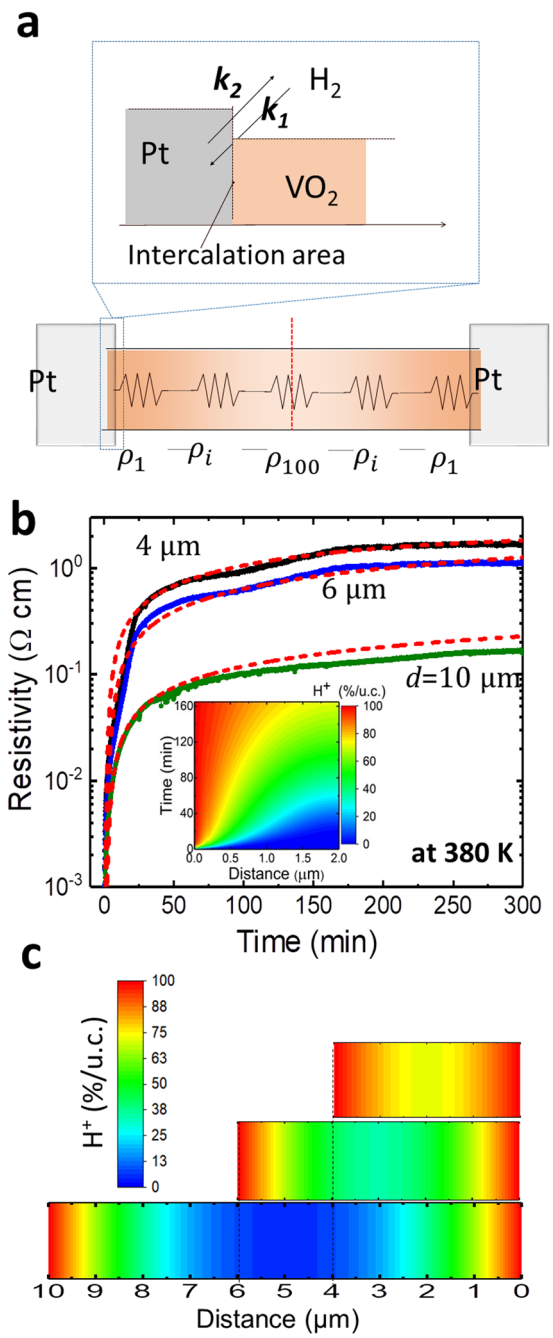

Figure 2. Transient electronic transport behaviors of VO_2 microwires in 4-μm-, 6-μm- and 10-μm-length. (**a**) Illustration of the chemical kinetics with forward (k_1) and reverse (k_2) reaction rate constants with the Pt catalytic effect (upper) and the serial resistor model via the FMD simulation. (**b**) Experimental and simulation results for the time dependence of the resistivity in 4-μm-, 6-μm-, and 10-μm-length VO_2 wires after starting hydrogen intercalation under the $H_2(5\%) + Ar(95\%)$ gas atmosphere at 380 K. The inset shows the spatiotemporal map of the proton ratio for the case of $D_{HVO2} = 150\ nm^2/s$, which was the fitting value for the doted lines of the 4-μm-, 6-μm-, and 10-μm-length VO_2 wires in Fig. 2b. (**c**) Spatial maps of the proton ratio using $D = 150\ nm^2/s$ in the 4-μm-, 6-μm-, and 10-μm-length VO_2 wires for 4 h after start from hydrogen intercalation.

[110] directions, respectively, because the diffusion constant of protons hopping to next oxygen sites is dependent on square length of $d_{o\text{-}o}$. The $d_{o\text{-}o}$ in TiO_2 [001] direction is approximately 1.48 Å[25], whereas the $d_{o\text{-}o}$ in VO_2 [110] and HVO_2 [110] are approximately 2.66 Å and 2.68 Å[13], respectively. Figure 2c shows the spatial mapping of the proton ratio using $D_{HVO2} = 150\ nm^2/s$ with 4-μm-, 6-μm-, and 10-μm-length VO_2 wires for 4 h after the start of proton intercalation. The occupancy of the protons was high at >80%/unit cell, even at the center of the 4-μm-length VO_2 wire, while the center of the 10-μm-length wire was still unoccupied by protons. The spatial density of HVO_2 clearly reflects the resistance behavior shown in Fig. 2b.

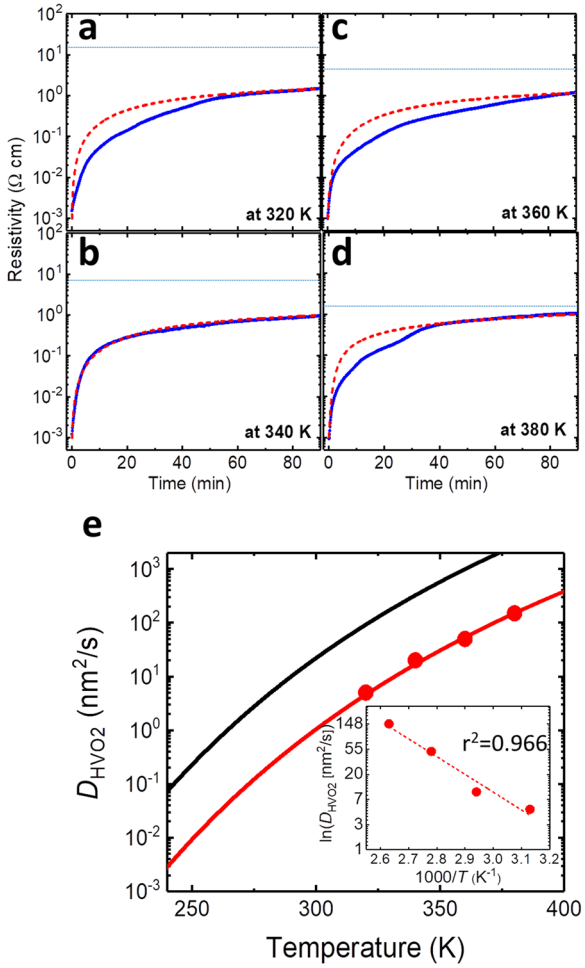

Figure 3. Transient electronic transport behaviors of the 4-μm-length VO_2 microwire at a variety of temperatures. (**a–d**) Time dependence of the resistivity behaviors in the 4-μm-length VO_2 wire at 320 K, 340 K, 360 K and 380 K, respectively. (**e**) the red dots represent experimental D_{HVO2} values in the VO_2 wire with structural transformation to HVO_2, estimated from the simulated fitting in Fig. 3a–d (the red dot lines). The red line is the fitting curve using Eq. (4). In comparison with the experimental D_{HVO2}, the proton diffusion constant of the parallel direction along the c axis of TiO_2 as a function of temperature in ref. [21] (black line). The inset shows the $1/T$ dependence of ln D_{HVO2} for the Arrhenius plots.

Discussion of the physical picture. Next, we estimated the activation energy (E_{HVO2}) for the structural transformation from VO_2 to HVO_2 using the experimental results of the 4-μm-length VO_2 wire and simulation fittings. Figure 3a–d show the time dependence of the resistivity behaviors in the 4-μm-length VO_2 wire at 320 K, 340 K, 260 K, and 380 K, respectively. The simulation curves (red dot curves) were fitted by appropriately selecting the D_{HVO2} values. The dashed blue lines in Fig. 3a–d indicate the resistivity of HVO_2 with the measurement temperature taken from the 4-μm-length VO_2 wire in Fig. 1b. The values of the experimental resistivity at each temperature were used as the simulation values of $\rho_i^{HVO2}(T)$. From these fittings, we estimated the D_{HVO2} values, which are 5 nm²/s at 320 K, 10 nm²/s at 340 K, 50 nm²/s at 360 K, and 150 nm²/s at 380 K, respectively. In general, the variation of the diffusion constant (D) with temperature takes the form of a thermally activated-type equation as below:

$$D(T) = D_0 \exp\left(-\frac{E_D}{k_B T}\right). \quad (4)$$

where E_D is the diffusive activation energy and D_0 is the frequency factor.

Figure 3e shows temperature dependence of D_{HVO2}. The red dots represent the experimental D_{HVO2} values in the VO_2 wire with structural transformation to HVO_2, estimated from the simulated red dot lines in Fig. 3a–d. The red line is the fitting curve using Eq. (4). Compared with our experimentally determined D_{HVO2} values, the diffusion constant of protons in the direction parallel to the c axis of rutile-TiO_2 (black line)[18] are reasonably similar. Considering the diffusion constant of protons in TiO_2[25], which is same crystal structure as VO_2, and the direct observation of proton diffusion in VO_2 by a microscope[15]. In addition, at the section D in

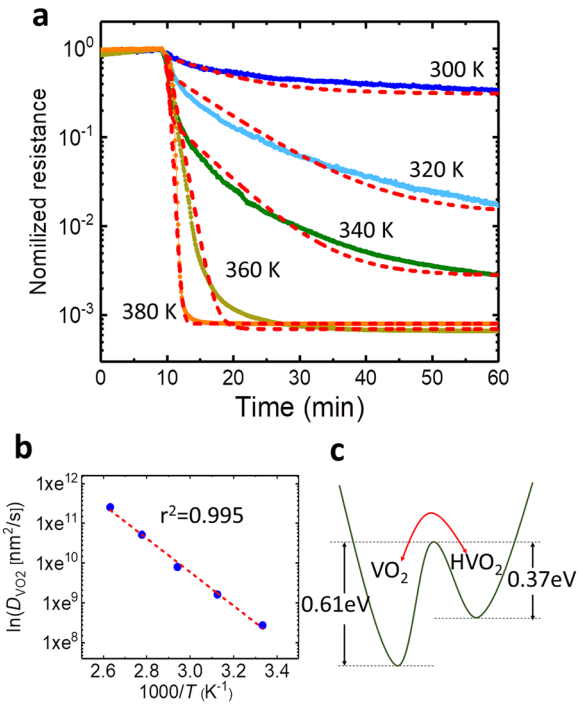

Figure 4. Transient electronic transport behaviors returned from HVO_2 to VO_2. (**a**) Time dependence of normalized-resistive behaviors from HVO_2 to VO_2 under a N_2 gas atmosphere in the 4-μm-length wire at 300 K, 320 K, 340 K, 360 K, and 380 K, respectively. The red dot lines show simulation curves derived by Eqs. Eq. (1–4) including the inhabitant effect in Section B of Supplementary Information. (**b**) The $1/T$ dependence of ln D_{VO2} for the Arrhenius plots. (**c**) Schematic of the crystal transformation energies between VO_2 and HVO_2.

Supplementary Information, resistance once insulating monoclinic-state of VO_2 at 290 K decreases in an insulating monoclinic-state of VO_2 at 290 K under a $H_2(5\%) + Ar(95\%)$ gas atmosphere. This is due to carrier doping from OH group without crystal transformation, that is, carrier density increases keeping the tetragonal VO_2 structure. With further developing proton-intercalation, the heavy proton dopants promote transformation to the different crystal structure of insulating HVO_2[13]. This transient response appears in Fig. S4. Thus, the origin of resistance changes in Figs. 2b, 3a–d and 4a can be more reasonably explained as proton diffusion in VO_2 than formation of contact resistance and/or small fractions having proton-puddles. The inset shows the $1/T$ dependence of ln D_{HVO2} for the Arrhenius plots. Figure 3e shows $1/T$ dependence of the D_{HVO2} values derived from the fitting curves using Eq. (4). The solid red line was obtained by the least-square method. From the slope, we determined that the diffusive activation energy for transformation from VO_2 to HVO_2 was 0.61 eV. For the diffusive activation energy for the reverse transformation from HVO_2 to VO_2, we estimated the diffusion coefficients ($D_{VO2}(T)$). Figure 4a shows the transient normalized-resistance curves for the reverse HVO_2 to VO_2 transformation in a N_2 atmosphere at 300 K, 320 K, 340 K, 360 K, and 380 K, respectively. Simulation curves using the FDM calculations could be well fitted to the experimental curves by incorporating the temperature-dependent coverage of hydrogen adatoms on Pt surface[26] (Section B of the Supplementary Information provides further details). The D_{VO2} was 4600 nm^2/s at 300 K, 10000 nm^2/s at 320 K, 20000 nm^2/s at 340 K, 45000 nm^2/s at 360 K, and 90000 nm^2/s at 380 K, which were more than two orders higher than those of D_{HVO2}. From the fitted D_{VO2} at various temperatures, the activation energy for the transformation from HVO_2 to VO_2 (E_{VO2}) was determined to be 0.37 eV, as obtained from the slope in Fig. 4b. Figure 4(c) shows the transformation energy between VO_2 and HVO_2 derived from the above data. VO_2 structure is more stable than that in HVO_2 structure.

Discussion

We clarified the physical parameters of heavily proton-intercalated VO_2 through investigation of proton diffusion. Single-crystal VO_2 thin films with a layer-by-layer growth were used to describe the crystal transformation energies from VO_2 to HVO_2 and from HVO_2 to VO_2. This was accomplished through investigation of the proton diffusion using the basic equations listed in Eq. (1) to Eq. (3). Data from in-plane poly-crystalline VO_2 thin films with grains on Al_2O_3 (0001) substrates[27] were not well-fitted to the ideal simulations using these equations. This was because a different crystal direction in-plane and grain boundaries disturb the ideal proton diffusion (Section C in Supplementary Information provides further details). It was found that the proton diffusion speed from HVO_2 to VO_2 was approximately two orders higher than that for VO_2 to HVO_2. The long-range micro-meter proton propagation, differences in the proton diffusion constants, and the asymmetry transformation energy between HVO_2 and VO_2 offer opportunity for the realization of novel iontronic applications and for energy devices, such as hydrogen storage.

Methods

Microwire preparation. Single crystal VO_2 thin films were epitaxially grown on TiO_2 (001) substrates using the pulsed laser deposition technique (ArF excimer laser, $\lambda = 193$ nm), with a substrate temperature of 420 °C, an oxygen pressure of 0.95 Pa, a laser repetition rate of 2 Hz, and with an energy fluency of 10 mJ/cm^2. A V_2O_5 pellet was used as the target. The deposition rate was ~0.3 nm/min. The thickness of the VO_2 thin films were fixed at ~10 nm. VO_2 grown on the TiO_2 (001) substrate had a tetragonal (001) plane, which could be verified by the X-ray diffraction pattern and SEM images of the VO_2 thin films prepared under the same fabrication conditions in Ref. [28–30]. The films and Pt catalytic electrodes were patterned *via* photolithography. A 40-nm-thick Pt electrode was deposited on the patterned VO_2 microwires. The width (w) was fixed at 2 μm and the Pt electrode distance (d) was from 2 μm to 10 μm, as shown in the schematic in Fig. 1(a). The right image in Fig. 1a shows a VO_2 microwire with Pt electrodes as an example.

Measurements. The electronic properties of the films were measured via a two-probe method using a current-voltage source meter (2614B, Keithley Instruments) under $H_2(5\%) + Ar(95\%)$ or N_2 gas atmospheres. The current flow direction was [110] in the rutile VO_2 thin films.

Received: 28 August 2019; Accepted: 13 December 2019;
Published online: 27 December 2019

References

1. Fisher, B. Electrical and Seebeck effect measurements in Nb-doped VO_2. *J. Phys. Chem. Solid.* **43**, 205–211 (1982).
2. Takahashi, I., Hibino, M. & Kudo, T. Thermochromic properties of double-doped VO2 thin films prepared by a wet coating method using Polyvanadate-based sols contacting W and Mo or W and Ti. *Jpn. J. Appl. Phys.* **40**, 1391–1395 (2001).
3. Shibuya, K., Kawasaki, M. & Tokura, Y. Metal-insulator transition in epitaxial $V_{1-x}W_xO_2(0\leq x\leq 0.33)$ thin films. *Appl. Phys. Lett.* **96**(1-3), 022102 (2010).
4. Miyazaki, K., Shibuya, K., Suzuki, M., Wado, H. & Sawa, A. Correlation between thermal hysteresis width and broadening of metal–insulator transition in Cr- and Nb-doped VO_2 films. *Jpn. J. Appl. Phys.* **53**(1-5), 071102 (2014).
5. Strelcov, E. *et al*. Doping-Based Stabilization of the M2 Phase in Free-Standing VO_2 Nanostructures at Room Temperature,. *Nano Lett.* **12**, 6198–6205 (2012).
6. Ardakani, H. A. *et al*. Atomic Origins of Monoclinic-Tetragonal (Rutile) Phase Transition in Doped VO_2 Nanowires. *Nano Lett.* **15**, 7179–7188 (2015).
7. Shibuya, K., Kawasaki, M. & Tokura, Y. Metal-insulator transition in epitaxial $V_{1-x}W_xO_2(0\leq x\leq 0.33)$thin films. *Appl. Phys. Lett.* **96**(1-3), 022102 (2010).
8. Liu, S. J., Fang, H. W., Su, Y. T. & Hsieh, J. H. Metal–insulator transition characteristics of Mo- and Mn-doped VO_2 films fabricated by magnetron cosputtering technique. *Jpn. J. Appl. Phys.* **53**(063201), 1–5 (2014).
9. Takami, H., Kanki, T., Ueda, S., Kobayashi, K. & Tanaka, H. Filling-controlled Mott transition in W-doped VO_2. *Phys. Rev. B* **85**(1-4), 205111 (2012).
10. Takami, H., Kawatani, K., Kanki, T. & Tanaka, H. High Temperature-Coefficient of Resistance at Room Temperature in W-Doped VO_2 Thin Films on Al_2O_3 Substrate and Their Thickness Dependence. *Jpn. J. Appl. Phys.* **50**(055804), 1–3 (2011).
11. Wei, J., Ji, H., Guo, W., Nevidomskyy, A. H. & Natelson, D. Hydrogen stabilization of metallic vanadium dioxide in single-crystal nanobeams. *Nature Nanotech.* **7**, 357–362 (2012).
12. Shi, J., Zhou, Y. & Ramanathan, S. Colossal resistance switching and band gap modulation in a perovskite nickelate by electron doping. *Nat. Commun.* **5**(5860), 1–9 (2013).
13. Yoon, H. *et al*. Reversible phase modulation and hydrogen storage in multivalent VO_2 epitaxial thin films. *Nature Mater.* **15**, 1113–1120 (2016).
14. Chen, Y. *et al*. Non-catalytic hydrogenation of VO_2 in acid solution. *Nat. Commun.* **9**(1-8), 818 (2018).
15. Lin, J. *et al*. Hydrogen Diffusion and Stabilization in Single-Crystal VO_2 Micro/ Nanobeams by Direct Atomic Hydrogenation. *Nano Lett.* **14**, 5445–5451 (2014).
16. Ohta, H. *et al*. Field-induced water electrolysis switches an oxide semiconductor from an insulator to a metal. *Nat. Commun.* **1**(1-6), 118 (2010).
17. Sasaki, T., Ueda, H., Kanki, T. & Tanaka, H. Electrochemical gating-induced reversible and drastic resistance switching in VO_2 nanowires. *Sci. Rep.* **5**(1-7), 17080 (2015).
18. Kanki, T. & Tanaka, H. Research Update: Nanoscale electrochemical transistors in correlated oxides. *APL Mater.* **5**(1-11), 042303 (2017).
19. Ji, H., Wei, J. & Natelson, D. Modulation of the Electrical Properties of VO_2 Nanobeams Using an Ionic Liquid as a Gating Medium. *Nano Lett.* **12**, 2988–2992 (2012).
20. Jo, M. *et al*. Gate-Induced Massive and Reversible Phase Transition of VO_2 Channels Using Solid-State Proton Electrolytes. *Adv. Funct. Mater.* **28**(1-7), 1802003 (2018).
21. Filinchuk, Y. *et al*. *In Situ* Diffraction Study of Catalytic Hydrogenation of VO_2: Stable Phases and Origins of Metallicity. *J. Am. Chem. Soc.* **136**, 8100–8109 (2014).
22. Hong, W.-K. *et al*. Hydrogen-Induced Morphotropic Phase Transformation of Single-Crystallin Vanadium Dioxide Nanobeams. *Nano Lett.* **13**, 1822–1828 (2013).
23. Lin, J. *et al*. Hydrogen Diffusion and Stabilization in Single-Crystal VO_2 Micro/Nanobeams by Direct Atomic Hydrogenation. *Nano Lett.* **14**, 5445–5451 (2014).
24. Warnick, H. K., Wang, B. & Pantelides, T. S. Hydrogen dynamics and metallic phase stabilization in VO_2. *Appl. Phys. Lett.* **104**(1-4), 101913 (2014).
25. Bates, J. B., Wang, J. C. & Perkins, R. A. Mechanisms for hydrogen diffusion in TiO_2. *Phys. Rev. B* **19**, 4130–4139 (1979).
26. Markovic, N. M., Grgur, B. N. & Ross, P. N. Temperature-Dependent Hydrogen Electrochemistry on Platinum Low-Index Single-Crystal Surfaces in Acid Solutions. *J. Phys. Chem. B* **101**, 5405–5413 (1997).
27. Okimura, K. & Sakai, J. Changes in Lattice Parameters of VO_2 Films Grown on c-Plane Al_2O_3 Substrates across Metal–Insulator Transition,. *Jpn. J. Appl. Phys.* **48**(1-6), 045504 (2009).
28. Wei, T., Kanki, T., Fujiwara, K., Chikanari, M. & Tanaka, H. Electric field-induced transport modulation in VO_2 FETs with high-k oxide/organic parylene-C hybrid gate dielectric. *Appl. Phys. Lett.* **108**(1-4), 053503 (2016).
29. Sohn, A., Kanki, T., Sakai, K., Tanaka, H. & Kim, D. W. Fractal Nature of Metallic and Insulating Domain Configurations in a VO_2 Thin Film Revealed by Kelvin Probe Force Microscopy. *Sci. Rep.* **5**(1-7), 10417 (2015).
30. Kawatani, K., Kanki, T. & Tanaka, H. Formation mechanism of a microscale domain and effect on transport properties in strained VO_2 thin films on TiO_2(001). *Phys. Rev. B* **90**(1-5), 054203 (2014).

Acknowledgements
The authors would like to thank S. Sakakihara for carrying out the RIE process, M. Sakuma for advice on proper device-preparation methods, Professor H. Tanaka for giving comments in this paper, and the Nanotechnology Platform Project (Nanotechnology Open Facilities in Osaka University) from the Ministry of Education, Culture, Sports, Science and Technology, Japan (MEXT) (S-18-OS-0020, F-18-OS-0024). This work was performed under the Cooperative Research Program of "Network Joint Research Center for Materials and Devices".

Author contributions
K.M. fabricated the devices, conducted the measurements, analyzed the data, and wrote the manuscript. T.K. planned the research direction, supervised the experiment, analyzed the data, and the main manuscript text. All authors reviewed the manuscript.

Competing interests
The authors declare no competing interests.

Additional information
Supplementary information is available for this paper at https://doi.org/10.1038/s41598-019-56685-4.

Correspondence and requests for materials should be addressed to T.K.

Reprints and permissions information is available at www.nature.com/reprints.

Publisher's note Springer Nature remains neutral with regard to jurisdictional claims in published maps and institutional affiliations.

Open Access This article is licensed under a Creative Commons Attribution 4.0 International License, which permits use, sharing, adaptation, distribution and reproduction in any medium or format, as long as you give appropriate credit to the original author(s) and the source, provide a link to the Creative Commons license, and indicate if changes were made. The images or other third party material in this article are included in the article's Creative Commons license, unless indicated otherwise in a credit line to the material. If material is not included in the article's Creative Commons license and your intended use is not permitted by statutory regulation or exceeds the permitted use, you will need to obtain permission directly from the copyright holder. To view a copy of this license, visit http://creativecommons.org/licenses/by/4.0/.

© The Author(s) 2019